Ultrathin Sulfide/PVDF-HFP Composite Electrolyte for Solid-State Sodium Metal Batteries

Xiaolin Guo [a], Yang Li [a], Hui Wang*, [a]

a. Mechanical Engineering Department, University of Louisville, KY, US, 40292

Corresponding Author: hui.wang.1@louisville.edu

Abstract

Rechargeable solid-state sodium batteries that utilize solid electrolytes (SEs) have garnered considerable attention due to their enhanced safety abundant sodium resources. Solid composite electrolytes (SCEs) that disperse the fine ceramic particles in a polymer matrix, provide a viable approach to address these challenges. Nevertheless, intensive efforts have been devoted on inorganic oxide-based conductors, while the studies on SCEs with sulfide-based Na-ion conductors are rarely reported. In this work, we report the preparation of ultra-thin, flexible, and stable SCE with adjustable thickness (20-65 μm) by embedding micro-sized Na_3SbS_3Se (NSSE) particles in a polymer (PVDF-HFP) matrix. The NSSE-SCE exhibits the highest ionic conductivity of 1.31×10^{-4} S cm^{-1} at room temperature, one order higher than that of polymer electrolyte. In addition, the critical current density (CCD) for 20 μm NSSE-SCE membrane is estimated to be 1.1 mA cm^{-2}. The assembled Na|SCE|TiS_2 solid-state batteries with the thinnest thickness demonstrates the best electrochemical performance, which delivers a discharge capacity of 182 mA h g^{-1} and shows stable cycling up to 300 cycles, as well as great rate performance. This work presents solid composite electrolyte with sulfide-based Na-ion conductors and contribute to the development of solid-state Na metal batteries.

Keywords:

Ultra-thin, Solid Composite Electrolytes, Na-ion Conduction, Sulfide, Solid-state Batteries

1. Introduction

Rechargeable batteries based on sodium (Na) electrochemistry have attracted considerable interest attentions for energy storage systems at the medium or grid scale, mainly due to the abundance of sodium resources and acceptable electrochemical voltage range.[1, 2] Similar to their counterparts in lithium chemistry, conventional Na-ion batteries contain liquid organic electrolytes that are volatile and flammable, which could cause serious safety concerns.[3, 4] Instead, utilizing solid-state conductors as SEs is considered to effectively address such safety issues due to their feature of intrinsic non-flammability.[5] Moreover, the use of SEs also enable to utilize anode materials with high energy density (i.e. Na metal, theoretical capacity of 1,166 mA h g^{-1}),[6-8] leading to advanced solid-state sodium batteries (SSSBs) with high potential on both high energy density and enhanced safety.

So far, popular ceramic SEs include oxides (e.g. $Na_3Zr_2Si_2PO_{12}$) [9], sulfides (e.g. Na_3PS_4 and Na_3SbS_4),[10-12] and halides (e.g., Na_3YCl_6),[13] etc. Among them, Na_3SbS_4-family SEs have attracted intense attention due to their advantages of high ionic conductivity ($10^{-4} \sim 10^{-2}$ S cm^{-1}), densification *via* cold-pressing, and straightforward synthesis methods.[14-16] Doping chemistry (e.g., W^{6+}, Se^{2-}, and Cl^-)[17-19] has been explored in Na_3SbS_4-family conductors. Nevertheless, they are still facing one main challenge of poor stability towards Na metal, which impedes the practical applications of Na_3SbS_4-family conductors in SSSBs.

Solid composite electrolytes (SCEs) involve a homogeneous dispersion of ceramic particles into a polymeric matrix. Solid polymer electrolytes include poly(ethylene oxide) (PEO),[20] poly(vinylidene fluoride) (PVDF),[21] poly(methyl methacrylate) (PMMA),[22] and

polyacrylonitrile (PAN),[23] etc. They are highly flexible but show low ionic conductivity (10^{-5} S cm^{-1}).[24, 25] SCEs are designed to combine the individual advantages of ceramic (e.g. fast ion-transport, mechanically robust) and polymer (e.g. high stability and flexible).[26, 27] We previously demonstrated Li_7PS_6-incorporated SCEs to display an ionic conductivity of 1.1 × 10^{-4} S cm^{-1} and a stable battery cycling in $LiFePO_4$||Li batteries.[28]

The state-of-the-art research on SCEs in Na batteries mostly focused on oxide as inorganic component, for examples, $Na_3Zr_2Si_2PO_{12}$/PEO,[29-31] $Na_3Zr_2Si_2PO_{12}$/PVDF,[32] and Ga-doped $Na_2Zn_2TeO_6$/PEO,[33] and beta-Al_2O_3/PVDF–HFP,[34] etc. Nevertheless, the SCEs that containing sulfides are rarely reported except few literatures, such as Na_3PS_4/PEO [35] and Na_3SbS_4/PEO [36] composites. These discoveries strongly indicate the great promise of composites containing sulfides in SSSBs.

Herein, we report the synthesis of Na_3SbS_3Se (NSSE)/PVDF-HFP SCE membranes by embedding micro-sized NSSE particles into a matrix of PVDF-HFP/$NaPF_6$ to obtain ultra-thin SCE membranes with adjustable thickness (20~65 μm). The prepared SCEs with 10 wt% NSSE exhibits the highest ionic conductivity of 1.31 × 10^{-4} S cm^{-1} at room temperature, twelve times higher than that of polymer electrolyte (PVDF-HFP/$NaPF_6$). The critical current density (CCD) value for the thinnest NSSE-SCE (20 μm) is estimated to 1.1 mA cm^{-2} from Na symmetric cells. Moreover, ultra-thin NSSE-SCE also yields to the best electrochemical performance than thicker thickness of SCEs. The fabricated Na|SCE|TiS_2 SSBs display an initial discharge capacity of 182 mAh g^{-1} at a current density of 200 mA g^{-1} and a good capacity retention up to 300 cycles, as well as great rate performance for current density up to 200 mA g^{-1}. This works demonstrates novel sulfide SCEs and their feasibility in Na batteries, paving the pathway for

the development next generation low cost and efficient batteries.

2. Experimental Section

2.1 Synthesis of Na_3SbS_3Se and preparation of composite Electrolyte

The Na_3SbS_3Se **(**NSSE) powder was synthesized by a solvent-free and low temperature heating method.[37] The produced NSSE power was further ball milled to obtain fine powder. The process to prepare a solid composite electrolyte (SCE) membrane includes three steps. *First*, PVDF-HFP (Mw: 400,000, Sigma-Aldrich) and $NaPF_6$ (Sigma) (2:1 weight ratio) were dissolved in a THF solvent to form a transparent solution. *Second*, a certain amount of inorganic NSSE powder (0, 5, 10, 15, 20 wt%) was added in above solution and followed by vigorous stirring to form a homogeneous mixture. *Third*, the mixture was casting onto a Teflon dish and then dried at 40˚C for 12 h to evaporate the solvent to obtain the final freestanding SCE membranes (NSSE/PVDF-HFP/$NaPF_6$). During the preparation process, the volume of mixture solution can be controlled to produce SCE membranes with different thickness (20-65 μm).

2.2 Materials Characterization

The phase structures of NSSE powder, PVDF-HFP polymer, and NSSE/PVDF-HFP as well as NSSE/PVDF-HFP/$NaPF_6$ samples were characterized by X-ray diffraction instrument (Bruker D8 Discover) equipped with Cu Kα radiation (λ= 1.5418 Å) within the range of 2θ= 10º~ 70º. Raman spectra of these samples were obtained by a Renishaw inVia Raman/PL Microscopy with 632.8 nm laser. For the SCE membrane (10 wt%NSSE/PVDF-HFP/$NaPF_6$), its surface and cross-sectional morphology was examined by TESCAN scanning electron microscopy coupled with energy dispersive spectroscopy (EDS) for elemental mapping. After electrochemical cycling, the cells were disassembled, and X-ray photoelectron spectroscopy

(XPS, Thermo VG Scientific) was performed to analyze the interface between SE and Na metal.

2.3 Electrochemical Measurements

For the prepared SCE membranes with different contents of NSSE, their ionic conductivities were evaluated by electrochemical impedance spectroscopy (EIS) on a potentiostat (Biologic VSP300) in the frequency range from 5 MHz to 0.1 Hz. The sodium-ion conductivity of the solid-state electrolyte was calculated by $\sigma = \frac{L}{A \times R}$, where σ refers to the ionic conductivity, L is the thickness of the electrolyte, A is the area of the membrane, R is the impedance of the membrane from Nyquist plots. The temperature dependence of ionic conductivity was collected by the combination with a temperature controller chamber to obtain the Arrhenius plots from 30 to 80 °C at an interval of 10 °C. The Na||Na symmetric cells were assembled by sandwiching the SCE membrane between two Na foil (area: 1.266 cm^2, thickness: ~150 μm) in 2032-coin cells, and then cycled using a potentiostat under a certain current density of 0.1 mA cm^{-2} (0.05 mAh cm^{-2}). The Na||Na symmetric cells were also used to measure the transference number of the membrane by a direct-current (DC) polarization and alternate-current (AC) impedance method. The polarization voltage was controlled to be 10 mV. The CCD tests were carried out under the initial current density of 0.01 mA cm^{-2} for 3 cycles and then one cycle under each current density from 0.02, 0.03, 0.05, 0.1, 0.2 to 1.2 mA cm^{-2} with an interval of 0.1 mA cm^{-2}. The linear sweeping voltammetry (LSV) measurement was conducted with the structure of solid electrolytes sandwiched with Na metal and stainless steel (SS) at a scanning rate of 1 mV/s.

For the TiS_2||Na cells assembly, Na foil was used as the anode, and TiS_2 as the active material in the composite cathode. The TiS_2 composite cathodes were prepared by mixing the

commercial TiS_2 powder (99.8%, Strem Chemicals), acetylene black and PVDF binder (dissolved in N-methyl-2-pyrrolidone) in the weight ratio of 60:30:10 to form a homogeneous slurry, which was coated on aluminum foil and dry at 80 ˚C for overnight. The mass loading of active materials was about 1 mg/cm^2. In addition, 10 μL $NaPF_6$/EC-DMC electrolyte was added at interface to reduce the solid/solid contact resistance. The TiS_2|SCE|Na batteries were assembled in 2032-coin cell and cycled within the electrochemical voltage window of 1.4-3.0 V (vs. Na^+/Na) using NEWARE battery testing system. The cyclic voltammograms (CV) scanning of TiS_2||Na solid state batteries were carried out a scan rate of 0.1 mV s^{-1} within the potential range of 1.4-3.0 V. All the symmetric cell and battery assembly were carried out in the Argon-filled glovebox (low H_2O and O_2).

3. Results and Discussion

3.1. Structure and Morphology of NSSE-SCE membranes

To prepare thin SCE membranes, inorganic NSSE sample was ball milled to obtain fine particles. The particles size of NSSE is within range of 2-5 μm (**Figure S1**), and the EDS mapping shows a homogeneous distribution of sodium (Na), antimony (Sb), sulfur (S) and Selenium (Se). **Figure 1** presents the XRD patterns and Raman spectra of the synthesized SCE (NSSE/PVDF-HFP/$NaPF_6$), PVDF-HFP/$NaPF_6$, PVDF-HFP and NSSE. Unlike the tetragonal structure of Na_3SbS_4, the as-synthesized NSSE shows strong XRD diffraction patterns of 2θ = 17.5, 30.5 and 35°, corresponding to (110), (211), and (220) planes in cubic structure, which is consistent with the data reported by Xiong et al.[38] Pure PVDF-HFP sample shows two main peaks on 2θ = 19.6˚ and 21.2˚, and one broad peak on about 40˚. Adding sodium salt ($NaPF_6$) causes the left-shift of the main peaks of PVDF-HFP. For the SCE with both NSSE and Na salt,

the pattern shows the characteristic peaks of NSSE as indicated in the **Figure 1a**. It implies good compatibility among NSSE, PVDF-HFP and Na salt. As shown in **Figure 1b**, both PVDF-HFP/$NaPF_6$ and PVDF-HFP don't have obvious Raman peaks. In contrast, the Raman spectrum of NSSE displays three successive peaks ranging from 360 to 400 cm^{-1} that attributed to the symmetric and asymmetric stretching vibration of SbS_3Se group, which are similar to those in Na_3SbS_4 [10, 39]. In the SCE sample, the main characteristic peak at 360 cm^{-1} that from the SbS_3Se group in NSSE can be clearly observed. Therefore, the XRD and Raman results indicate that the crystalline and bonding structure of NSSE are well remained in the prepared SCEs.

The digital images of PVDF-HFP/$NaPF_6$ and NSSE/PVDF-HFP/$NaPF_6$ SCE are shown in **Figure 2a and b**, respectively. Although the polymer electrolyte membrane is clear and transparent (**Figure S2**), the SCE membrane has brown color due to the dark color of NSSE particles. The SEM images (**Figure 2c** and **d**) of the SCE membrane display a smooth and homogeneous surface morphology, although minor pores appear due to the evaporation of THF solvent during the preparation. The cross-sectional SEM image (**Figure 2e**) clearly shows that the thickness of SCE membrane is only ~20 μm, which is consistent with the measurement using caliper (**Figure S4**). This thickness of NSSE/PVDF-HFP/$NaPF_6$ SCE is comparable or even thinner than many other oxide-based composites (e.g. PI-LLZTO/PVDF (~20 μm) [40], LLZTO/PEO (~40 μm) [41]). Besides, the EDS mapping images (**Figure 2f**) show the elemental distribution of fluorine (F), sodium (Na), phosphorous (P), antimony (Sb), selenium (Se), and sulfur (S), which confirm the homogeneous distribution of fine NSSE particles in the SCE membrane. Additionally, **Figure S5 and S6** show the cross-sectional SEM images of thicker SCE membranes (40 μm, 65 μm), both membranes display dense morphology.

3.2. Na-ion conductivity of NSSE-SCE membranes

A series of SCE membranes were prepared to contain different contents of NSSE (0, 5, 10, 15, 20 wt%), and EIS measurements were employed on these samples to examine their ionic conductivities. **Figure 3a** presents the Nyquist plots of the SCE samples with different NSSE content at room temperature and the enlarged figure at high frequency part is shown in Figure S7. The Nyquist plots show a typical semi-circle at high frequency from the bulk resistance (R_b) of electrolytes and a spike at low frequency due to the blocking electrode. The resistance values clearly decrease after adding NSSE particles, suggesting the increased ionic conductivity of SCEs than polymer electrolyte (0 wt%). **Figure 3b** shows the composition dependence of ionic conductivity for the SCE membranes that contain different weight percents of NSSE. The PVDF-HFP/$NaPF_6$ sample (with 0 wt% NSSE) exhibits an ionic conductivity of 1.07×10^{-5} S cm^{-1}. After adding the inorganic NSSE particles, the SCE membranes show improved ionic conductivity and achieve the highest value of 1.31×10^{-4} S cm^{-1} at 10 wt.% NSSE. The enhanced ionic conductivity is because the presence of NSSE particles decrease the crystallinity of polymer and potentially provide additional conductive channels.[42] Beyond 10 wt% NSSE in SCEs, further increasing the ceramic content decreases the ionic conductivity, which is probably due to the aggregation of NSSE particles and the blocking of Na-ion transport.[43] Notley, all NSSE-SCE samples show higher ionic conductivity than that of polymer electrolyte although lower than that of pure NSSE.[37]

Figure 3c compares the temperature dependence of the SCE membrane with 10 wt% NSSE and polymer electrolyte (PVDF-HFP/$NaPF_6$) in the range of 30 to 80 °C. For both samples, it is observed linear behavior of Arrhenius plots according to the equation: $\sigma =$

$\sigma_0 \exp\left(-\frac{E_a}{kT}\right)$, where σ is the ionic conductivity, σ_0 is the pre-exponential factor, E_a is the activation energy, k is the Boltzmann constant, T is the Kelvin temperature. However, the SCE membrane shows an activation energy (E_a) of 0.31 eV, much lower than that of PVDF-HFP/$NaPF_6$ (0.6 eV). The lower activation energy in SCE sample is related to its conduction mechanisms, where Na-ions can be possibly transported through two approaches of polymer-polymer and ceramic-polymer.[44] The Nyquist plots of SCE tested at 30, 50 and 70 °C (**Figure S8**) show that the impedance decreases continuously as the temperature increases . In addition, the transference number (t_{Na^+}) of the SCE is calculated by the Bruce-Vincent equation: $t_{Na^+} = \frac{I_{ss}(\Delta V - I_0 R_0)}{I_0(\Delta V - I_{ss} R_{ss})}$, where I_0 and I_{ss} are the initial and steady currents, ΔV is a polarization voltage at 10 mV, R_0 and R_{ss} are the charge-transfer resistance of the symmetric cell before and after polarization, respectively.[45] The polarization profile and EIS before and after polarization are shown in **Figure S9**. After calculation, the t_{Na^+} was calculated to be 0.52, which is obviously higher than typical liquid electrolyte (0.2-0.4).[40] The increased transference number of SCE is related with the enhanced sodium ion transport by adding NSSE particles.

Figure S10 shows the linear sweep voltammetry curve of 10 wt% NSSE-SCE in comparison to that of polymer electrolyte (PVDF-HFP/$NaPF_6$). The electrochemical window of SCE is stable up to 4.9 V towards Na metal, which is higher than that of 4.3V for PVDF-HFP/$NaPF_6$. Na||Na symmetric cells were assembled to test the electrochemical compatibility of SCE toward Na metal in plating and stripping process. **Figure S11** compares the voltage profiles of the Na||Na symmetric cells with SCE and a polymer electrolyte under the same current density (0.1 mA cm^{-2}). Although the initial overpotential values of two cells are close, the cell with polymer electrolyte shows a larger polarization as the cycling precedes and finally

gets short after 50 cycles. In contrast, the Na|SCE|Na symmetric cell exhibits stable voltage profiles during the repeated Na plating/stripping process up to 100 hours with minor increase on the impedance during repeated cycling process. These results indicate that the NSSE-SCE shows an improved interfacial stability towards Na metal. **Figure 3d** shows the critical current density (CCD) test results of thin SCE membrane in comparison with the polymer electrolyte (PVDF-HFP/$NaPF_6$). The CCD value of thin SCE is estimated to 1.1 mA cm^{-2}, which is one order of magnitude than that of polymer electrolyte (0.1 mA cm^{-2}). Meanwhile, the overpotential values of SCE are obviously smaller than that of PVDF-HFP/$NaPF_6$ due to the higher ionic conductivity of SCE and good interface stability. The XPS spectra of C1s and F1s for 10 wt% NSSE-SCE exhibit much stronger NaF peak than that of polymer electrolyte (PVDF-HFP/$NaPF_6$), as shown in **Figure S12**. The presence of NaF at the interface is considered to contribute to the enhanced interfacial stability between NSSE-SCE and Na metal.

3.3 *Electrochemical stability characterization of NSSE-SCE with different thickness*

TiS_2||Na batteries were assembled to demonstrate the feasibility of SCEs in solid-state Na metal batteries. The composite cathode consists of TiS_2 as active material, PVDF (binder) and carbon black (conductive additive). **Figure 4a** compares the cycling performance of TiS_2||Na batteries with three different thickness of SCEs (20, 40, and 65 μm) up to 180 cycles. The cells with thinner SCEs (20, 40 μm) display higher cycling capacity and better capacity retention than that of cell with thicker SCE (65 μm). As shown in **Figure 4b**, the batteries with different thickness of SCEs show close capacities around 176~182 mA h g^{-1} at the initial cycles. Nevertheless, as the cycling proceeds, larger polarization voltage and faster capacity in the cells with thicker SCE although they still show clear plateaus during the charge and discharge

process. At the 100th cycle (**Figure 4c**), the cells with 20 μm and 40 μm SCEs retains the discharge capacity of 128 and 120 mA h g^{-1}, while the 65 μm-SCE based cell exhibits much lower capacity value of 85 mA h g^{-1}. The capacity difference is getting more obvious at 180th cycle **(Figure S13)**. This comparison suggests that thinner SEs benefits for better electrochemical performance due to the shorter ion diffusion and transport pathway.[46]

Figure 4d depicts the CV curves of a TiS_2||Na with 20 μm-SCE at a scan rate of 0.1 mV s^{-1}. During the first cathodic scanning process in CV, there are two sharp reduction peaks at 1.5 and 1.98 V (vs. Na^+/Na), corresponding to two flat plateaus in the galvanostatic charge and discharge curves (**Figure 4b**), respectively. These two plateaus reflect two distinct phases during a two-step Na insertion reaction:[47-49] TiS_2 → Na_xTiS_2 ($0 < x < 0.4$) → Na_yTiS_2 ($0.4 < y < 0.8$), which is in highly agreement with previous report.[50] For the 2nd to 5th CV curves, the presence of multiple peaks within two distinct regions are a characteristic of Na-insertion/extraction process.[47] As shown in **Figure S14**, the specific discharge and charge capacity of the 1st cycle is 225 mA h g^{-1} and 185 mA h g^{-1}, respectively. The low coulombic efficiency at 1st cycle also reflects interfacial side reactions and partial irreversible intercalation of Na^+, which is consistent with the observation in CV curves. After that, the discharge/charge profiles of the 2nd cycles are almost identical with those at 5th and 10th cycles, except for the slightly difference on specific capacity.

3.4 Rate performance and Long-term cycling stability of NSSE-SCE in Na//TiS_2 batteries

Figure 5a presents the rate capability and charge/discharge curves of TiS_2|SCE|Na cell at different current densities. As expected, the specific discharge capacity decreases continuously as increasing the current density from 20 mA g^{-1} to 200 mA g^{-1}. Under a higher current density

(150 and 200 mA g^{-1}), the cell can still deliver a discharge capacity of 148 and 128 mA h g^{-1}, respectively. More importantly, when the current density returns back to 20 mA g^{-1}, the cell's discharge capacity can resume back to 156 mA h g^{-1} and remain above 142 mA h g^{-1} at 80th cycle. The corresponding reversible charge/discharge profiles in **Figure 5b** at various current density exhibit obvious three plateaus and low-voltage polarizations, indicating great electrochemical reversibility of TiS_2||Na battery.The long-term cyclic performances of the TiS_2|SCE|Na and TiS_2|PVDF-HFP/$NaPF_6$|Na cells under a current density of 50 mA h g^{-1} are displayed in **Figure 5c**. Despite the cell with PVDF-HFP/$NaPF_6$ shows an initial specific discharge capacity of 190 mA h g^{-1}, its capacity quicky decays after 20 cycles and drops to 31 mA h g^{-1} after 100 cycles (retention rate of 17%). In contrast, the TiS_2|SCE|Na cell shows much better and more stable cycling performance. It delivers a discharge capacity of 182 mA h g^{-1} at the 2nd cycle with a columbic efficiency at 99%. Moreover, the columbic efficiency maintained over 99.2% during the whole cycling process (300 cycles). After the repeated charge/discharge, the TiS_2||Na battery remains its specific discharge capacity of 160 mA h^{-1} and 100 mA h g^{-1} at the 100th cycle and 300th cycle, respectively.

4. Conclusion

In summary, we reported the preparation of ultrathin (~20 μm) and flexible SCEs by the dispersion of micro-sized NSSE in PVDF-HFP polymer electrolyte. With the optimized NSSE content, the SCE achieves the highest ionic conductivity of 1.31×10^{-4} S cm^{-1} at room temperature (12 times higher than that of polymer electrolyte) and an activation energy of 0.31 eV. Among different thickness (~20, 40, 65 μm), the thinnest SCE membrane results in the best battery cycling performance in solid-state Na||TiS_2 batteries, with its specific discharge capacity

of 182 mAh g^{-1} at 2nd cycle and 128 mAh g^{-1} at 100th cycle. Also, Na|SCE|TiS_2 batteries deliver a stable electrochemical cycling of up to 300 cycles at a current density of 50 mA h g^{-1} and great rate performance (up to 200 mA h g^{-1}). The features of ultra-thin, high ionic conductivity, and good interfacial compatibility enable the developed SCE to be a promising electrolyte candidate for the future use in solid-state sodium batteries.

Supporting Information.

Supporting information is available. Includes SEM images of NSSE particles, SCE membranes with different thickness, Digital photos of SCE membrane, EIS plots, LSV curves, XPS spectra, voltage profiles of Na symmetric cells, and charge/discharge profiles of TiS_2|SCE|Na batteries at different cycles.

ACKNOWLEDGEMENT

The authors thank the support from U.S. National Science Foundation awards No. 2047460. We also acknowledge the support from the Conn Center for Renewable Energy Research at University of Louisville.

Reference:

1. Nayak, P. K.; Yang, L.; Brehm, W.; Adelhelm, P., From Lithium-Ion to Sodium-Ion Batteries: Advantages, Challenges, and Surprises. *Angew Chem Int Ed Engl* **2018,** *57* (1), 102-120.

2. Chen, Y.; Zhao, B.; Yang, Y.; Cao, A., Toward High-Areal-Capacity Electrodes for Lithium and Sodium Ion Batteries. *Advanced Energy Materials* **2022,** *12* (44), 2201834.

3. Zhao, C.; Liu, L.; Qi, X.; Lu, Y.; Wu, F.; Zhao, J.; Yu, Y.; Hu, Y.-S.; Chen, L., Solid-State Sodium Batteries. *Advanced Energy Materials* **2018,** *8* (17), 170312.

4. Zhang, W.; Lu, J.; Guo, Z., Challenges and future perspectives on sodium and potassium ion batteries for grid-scale energy storage. *Materials Today* **2021,** *50*, 400-417.

5. Kim, J.-J.; Yoon, K.; Park, I.; Kang, K., Progress in the Development of Sodium-Ion Solid Electrolytes. *Small Methods* **2017,** *1* (10), 1700219.

6. Fan, L.; Wei, S.; Li, S.; Li, Q.; Lu, Y., Recent Progress of the Solid-State Electrolytes for High-Energy Metal-Based Batteries. *Advanced Energy Materials* **2018,** *8* (11), 1702657.

7. Zhou, W.; Li, Y.; Xin, S.; Goodenough, J. B., Rechargeable Sodium All-Solid-State Battery. *ACS Cent Sci* **2017,** *3* (1), 52-57.

8. Zhao, Y.; Adair, K. R.; Sun, X., Recent developments and insights into the understanding of Na metal anodes for Na-metal batteries. *Energy & Environmental Science* **2018,** *11* (10), 2673-2695.

9. Wang, X.; Liu, Z.; Tang, Y.; Chen, J.; Wang, D.; Mao, Z., Low temperature and rapid microwave sintering of Na3Zr2Si2PO12 solid electrolytes for Na-Ion batteries. *Journal of Power Sources* **2021,** *481, 228924*.

10. Wang, H.; Chen, Y.; Hood, Z. D.; Sahu, G.; Pandian, A. S.; Keum, J. K.; An, K.; Liang, C., An Air-Stable Na3 SbS4 Superionic Conductor Prepared by a Rapid and Economic Synthetic Procedure. *Angew Chem Int Ed Engl* **2016,** *55* (30), 8551-5.

11. Tian, Y.; Sun, Y.; Hannah, D. C.; Xiao, Y.; Liu, H.; Chapman, K. W.; Bo, S.-H.; Ceder, G., Reactivity-Guided Interface Design in Na Metal Solid-State Batteries. *Joule* **2019,** 3(4), 1037-1050.

12. Hayashi, A.; Noi, K.; Sakuda, A.; Tatsumisago, M., Superionic glass-ceramic electrolytes for room-temperature rechargeable sodium batteries. *Nat Commun* **2012,** *3*, 856.

13. Wang, C.; Liang, J.; Kim, J. T.; Sun, X., Prospects of halide-based all-solid-state batteries: From material design to practical application. *Science Advances* **2022,** *8* (36), eadc9516.

14. Zhang, D.; Cao, X.; Xu, D.; Wang, N.; Yu, C.; Hu, W.; Yan, X.; Mi, J.; Wen, B.; Wang,

L.; Zhang, L., Synthesis of cubic Na3SbS4 solid electrolyte with enhanced ion transport for all-solid-state sodium-ion batteries. *Electrochim Acta* **2018,** *259*, 100-109.

15. Rush, L. E.; Hood, Z. D.; Holzwarth, N. A. W., Unraveling the electrolyte properties of Na3SbS4 through computation and experiment. *Phys. Rev. Mater.* **2017,** *1* (7), 075405.

16. Li, Y.; Arnold, W.; Halacoglu, S.; Jasinski, J. B.; Druffel, T.; Wang, H., Phase-Transition Interlayer Enables High-Performance Solid-State Sodium Batteries with Sulfide Solid Electrolyte. *Advanced Functional Materials* **2021,** *31* (28), 2101636.

17. Wan, H.; Mwizerwa, J. P.; Han, F.; Weng, W.; Yang, J.; Wang, C.; Yao, X., Grain-boundary-resistance-less Na3SbS4-xSex solid electrolytes for all-solid-state sodium batteries. *Nano Energy* **2019,** *66*, 104109.

18. Yubuchi, S.; Ito, A.; Masuzawa, N.; Sakuda, A.; Hayashi, A.; Tatsumisago, M., Aqueous solution synthesis of Na3SbS4–Na2WS4 superionic conductors. *Journal of Materials Chemistry A* **2020,** *8* (4), 1947-1954.

19. Cao, H.; Yu, M.; Zhang, L.; Zhang, Z.; Yan, X.; Li, P.; Yu, C., Stabilizing Na3SbS4/Na interface by rational design via Cl doping and aqueous processing. *Journal of Materials Science & Technology* **2021,** *70*, 168-175.

20. Liu, Q.; Yu, T.; Yang, H.; Xu, S.; Li, H.; Chen, K.; Xu, R.; Zhou, T.; Sun, Z.; Li, F., Ion coordination to improve ionic conductivity in polymer electrolytes for high performance solid-state batteries. *Nano Energy* **2022,** *103, 107763*.

21. Chen, J.; Zhang, H.; Chen, H.; Xia, E.; Wu, Y.; Li, Z., PVDF-based electrolyte decorated by Li29Zr9Nb3O40 Li-ion conductor and electrochemical performance of related solid-state batteries. *Journal of Power Sources* **2022,** *548, 232109*.

22. Wang, S.; Hu, J.; Gui, X.; Lin, S.; Tu, Y., A Promising PMMA/m-MgO All-Solid-State Electrolyte for Lithium-Oxygen Batteries. *Journal of The Electrochemical Society* **2021,** *168* (2), 020514.

23. Cheng, H.; Yan, C.; Orenstein, R.; Dirican, M.; Wei, S.; Subjalearndee, N.; Zhang, X., Polyacrylonitrile Nanofiber-Reinforced Flexible Single-Ion Conducting Polymer Electrolyte for High-Performance, Room-Temperature All-Solid-State Li-Metal Batteries. *Advanced Fiber Materials* **2022,** *4* (3), 532-546.

24. Xue, Z.; He, D.; Xie, X., Poly(ethylene oxide)-based electrolytes for lithium-ion batteries. *Journal of Materials Chemistry A* **2015,** *3* (38), 19218-19253.

25. Wu, Y.; Li, Y.; Wang, Y.; Liu, Q.; Chen, Q.; Chen, M., Advances and prospects of PVDF based polymer electrolytes. *Journal of Energy Chemistry* **2022,** *64*, 62-84.

26. Li, Y.; Guo, X.; Wang, H., Solid Composite Electrolytes for Solid-State Alkali Metal Batteries. In *Solid State Batteries Volume 1: Emerging Materials and Applications*, American Chemical Society: 2022; Vol. 1413, pp 395-423.

27. Zhang, Z.; Zhang, Q.; Shi, J.; Chu, Y. S.; Yu, X.; Xu, K.; Ge, M.; Yan, H.; Li, W.; Gu, L.; Hu, Y.-S.; Li, H.; Yang, X.-Q.; Chen, L.; Huang, X., A Self-Forming Composite Electrolyte for Solid-State Sodium Battery with Ultralong Cycle Life. *Advanced Energy Materials* **2017,** *7* (4), 1601196.

28. Li, Y.; Arnold, W.; Thapa, A.; Jasinski, J. B.; Sumanasekera, G.; Sunkara, M.; Druffel, T.; Wang, H., Stable and Flexible Sulfide Composite Electrolyte for High-Performance Solid-State Lithium Batteries. *ACS Appl Mater Interfaces* **2020,** *12* (38), 42653-42659.

29. Yu, X.; Xue, L.; Goodenough, J. B.; Manthiram, A., A high-Performance All-Solid-State Sodium Battery with a Poly(ethylene oxide)-Na3Zr2Si2PO12 Composite Electrolyte. *ACS Materials letters* **2019,** *1*, 132-138.

30. Wang, Y.; Wang, Z.; Sun, J.; Zheng, F.; Kotobuki, M.; Wu, T.; Zeng, K.; Lu, L., Flexible, stable, fast-ion-conducting composite electrolyte composed of nanostructured Na-super-ion-conductor framework and continuous Poly(ethylene oxide) for all-solid-state Na battery. *Journal of Power Sources* **2020,** *454*, 227949.

31. Niu, W.; Chen, L.; Liu, Y.; Fan, L.-Z., All-solid-state sodium batteries enabled by flexible composite electrolytes and plastic-crystal interphase. *Chemical Engineering Journal* **2020,** *384*, 123233.

32. Cheng, M.; Qu, T.; Zi, J.; Yao, Y.; Liang, F.; Ma, W.; Yang, B.; Dai, Y.; Lei, Y., A hybrid solid electrolyte for solid-state sodium ion batteries with good cycle performance. *Nanotechnology* **2020,** *31* (42), 425401.

33. Wu, J.-F.; Yu, Z.-Y.; Wang, Q.; Guo, X., High performance all-solid-state sodium batteries actualized by polyethylene oxide/Na2Zn2TeO6 composite solid electrolytes. *Energy Storage*

Materials **2020,** *24*, 467-471.

34. Lai, H.; Lu, Y.; Zha, W.; Hu, Y.; Zhang, Y.; Wu, X.; Wen, Z., In situ generated composite gel polymer electrolyte with crosslinking structure for dendrite-free and high-performance sodium metal batteries. *Energy Storage Materials* **2023,** *54*, 478-487.

35. Xu, X.; Li, Y.; Cheng, J.; Hou, G.; Nie, X.; Ai, Q.; Dai, L.; Feng, J.; Ci, L., Composite solid electrolyte of Na3PS4-PEO for all-solid-state SnS2/Na batteries with excellent interfacial compatibility between electrolyte and Na metal. *Journal of Energy Chemistry* **2020,** *41*, 73-78.

36. Wang, Z.; Zhang, L.; Shang, X.; Wang, W.; Yan, X.; Yu, C.; Wang, L.-m., Enhanced electrochemical performance enabled by ionic-liquid-coated Na3SbS4 electrolyte encapsulated in flexible filtration membrane. *Chemical Engineering Journal* **2022,** *428, 132094*.

37. Halacoglu, S.; Li, Y.; Arnold, W.; Shreyas, V.; Guo, X.; Jasinski, J. B.; Narayanan, B.; Wang, H., Solvent-free and low temperature synthesis of chalcogenide Na superionic conductors for solid-state batteries. *Chemical Engineering Journal* **2023,** *468*, 143624.

38. Xiong, S.; Liu, Z.; Rong, H.; Wang, H.; McDaniel, M.; Chen, H., Na3SbSe4-xS x as Sodium Superionic Conductors. *Sci Rep* **2018,** *8* (1), 9146.

39. Li, Y.; Arnold, W.; Halacoglu, S.; Jasinski, J. B.; Druffel, T.; Wang, H., Phase-Transition Interlayer Enables High-Performance Solid-State Sodium Batteries with Sulfide Solid Electrolyte. *Advanced Functional Materials* **2021,** *31* (28), 2101636.

40. Hu, J.; He, P.; Zhang, B.; Wang, B.; Fan, L.-Z., Porous film host-derived 3D composite polymer electrolyte for high-voltage solid state lithium batteries. *Energy Storage Materials* **2020,** *26*, 283-289.

41. Zhang, J.; Zhao, N.; Zhang, M.; Li, Y.; Chu, P. K.; Guo, X.; Di, Z.; Wang, X.; Li, H., Flexible and ion-conducting membrane electrolytes for solid-state lithium batteries: Dispersion of garnet nanoparticles in insulating polyethylene oxide. *Nano Energy* **2016,** *28*, 447-454.

42. Zhang, Z.; Chen, H.; Hu, Z.; Zhou, S.; Zhang, L.; Luo, J., Ion conduction path in composite solid electrolytes for lithium metal batteries: from polymer rich to ceramic rich. *Frontiers in Energy* **2022,** *16* (5), 706-733.

43. Zheng, J.; Hu, Y. Y., New Insights into the Compositional Dependence of Li-Ion Transport in Polymer-Ceramic Composite Electrolytes. *ACS Appl Mater Interfaces* **2018,** *10* (4), 4113-

4120.

44. Yang, H.; Wu, N., Ionic conductivity and ion transport mechanisms of solid-state lithium-ion battery electrolytes: A review. *Energy Science & Engineering* **2022,** *10* (5), 1643-1671.

45. Chen, L.; Qiu, X.; Bai, Z.; Fan, L.-Z., Enhancing interfacial stability in solid-state lithium batteries with polymergarnet solid electrolyte and composite cathode framework. *Jorunal of Energy Chemistry* **2021,** *52*, 210-217.

46. Wan, J.; Xie, J.; Kong, X.; Liu, Z.; Liu, K.; Shi, F.; Pei, A.; Chen, H.; Chen, W.; Chen, J.; Zhang, X.; Zong, L.; Wang, J.; Chen, L. Q.; Qin, J.; Cui, Y., Ultrathin, flexible, solid polymer composite electrolyte enabled with aligned nanoporous host for lithium batteries. *Nat Nanotechnol* **2019,** *14* (7), 705-711.

47. Chaturvedi, A.; Edison, E.; Arun, N.; Hu, P.; Kloc, C.; Aravindan, V.; Madhavi, S., Two Dimensional TiS2 as a Promising Insertion Anode for Na-Ion Battery. *ChemistrySelect* **2018,** *3* (2), 524-528.

48. Newman, G. H., Ambient Temperature Cycling of an Na-TiS2 cell. *J._Electrochem._Soc.* **1980,** *127*, 3, 2097.

49. Liu, Y.; Wang, H.; Cheng, L.; Han, N.; Zhao, F.; Li, P.; Jin, C.; Li, Y., TiS2 nanoplates: A high-rate and stable electrode material for sodium ion batteries. *Nano Energy* **2016,** *20*, 168-175.

50. Ryu, H.-S.; Kim, J.-S.; Park, J.-S.; Park, J.-W.; Kim, K.-W.; Ahn, J.-H.; Nam, T.-H.; Wang, G.; Ahn, H.-J., Electrochemical Properties and Discharge Mechanism of Na/TiS2Cells with Liquid Electrolyte at Room Temperature. *Journal of The Electrochemical Society* **2012,** *160* (2), A338-A343.

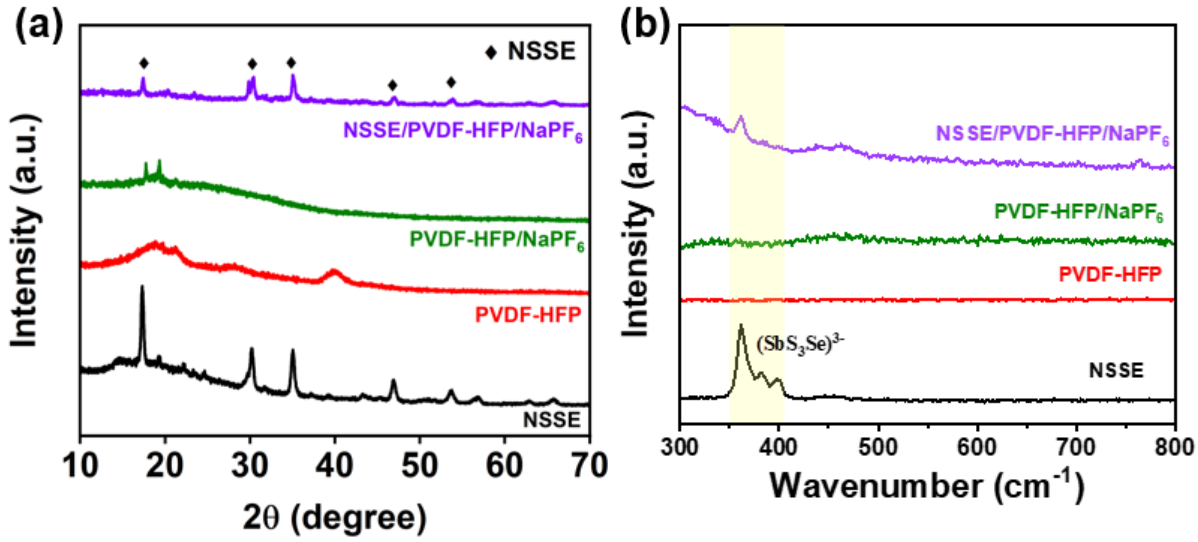

Figure 1. (a) XRD patterns and (b) Raman spectra of solid composite electrolyte (NSSE/PVDF-HFP/$NaPF_6$), polymer electrolyte (PVDF-HFP/$NaPF_6$), PVDF-HFP, and NSSE powder.

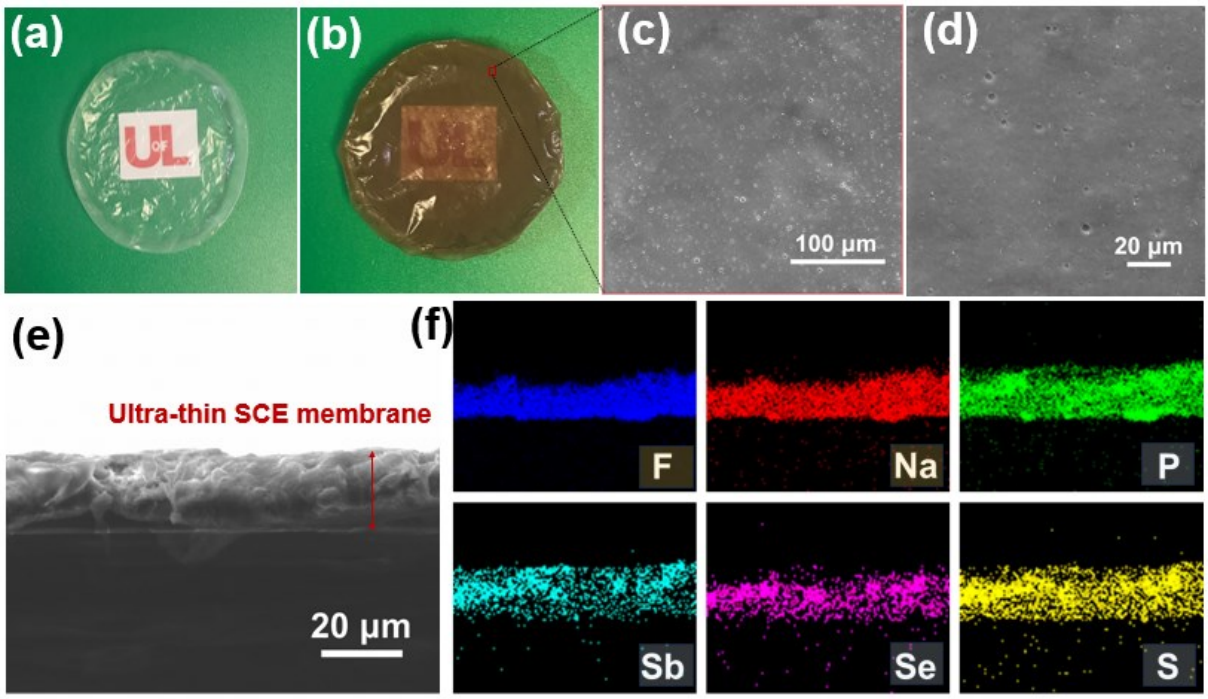

Figure 2. Digital images of (a) PVDF-HFP/$NaPF_6$ and (b) SCE membrane with 10 wt.% NSSE. SEM images (c) and (d) of top view of SCE membrane with different magnification. (e) and (f) Cross-sectional SEM image of an ultra-thin SCE membrane and its corresponding elemental mappings of F, Na, P, Sb, Se, S distribution in the SCE membrane. (Sb, Se, S elements come from Na_3SbS_3Se sulfide, F, P elements come from $NaPF_6$ salt, Na element come from both).

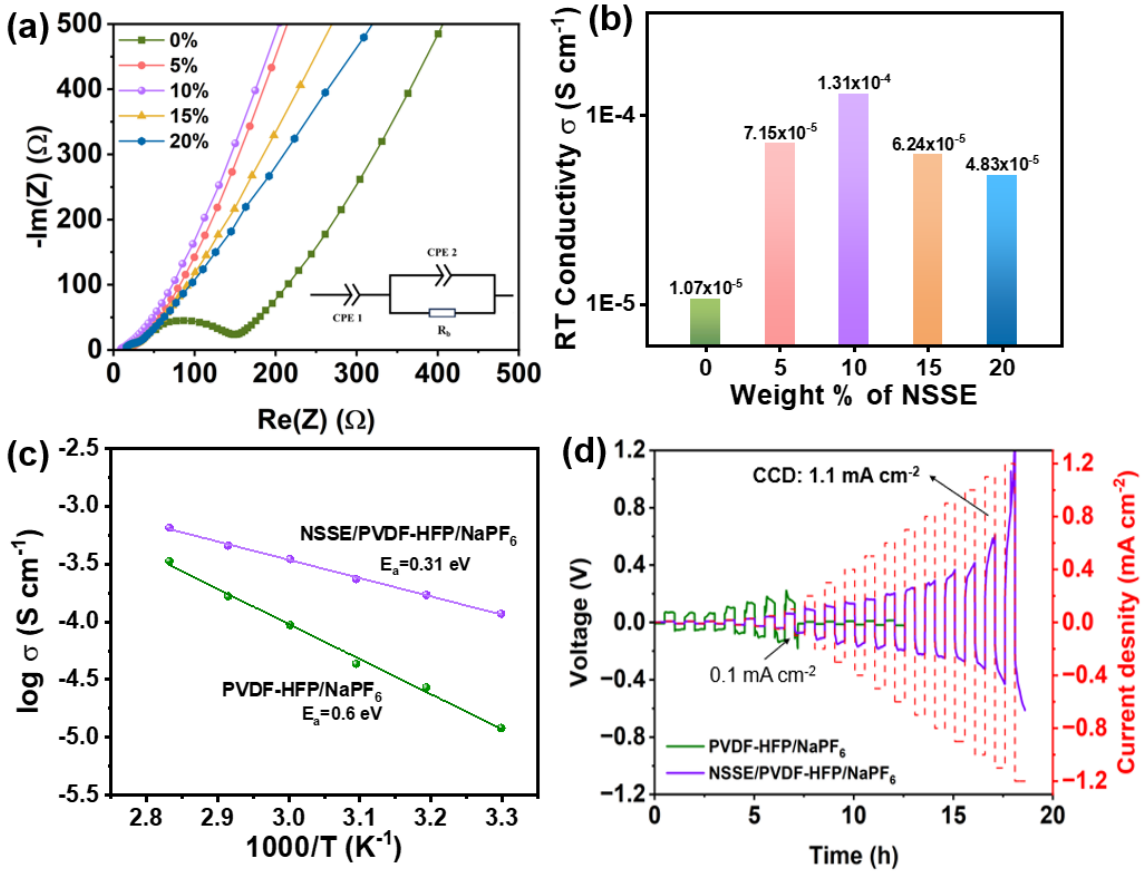

Figure 3. (a) Nyquist plots, (b) room temperature ionic conductivity of the SCE membranes with different weight% of NSSE (x=0, 5%, 10%, 15%, 20%), 0% represents polymer electrolyte (PVDF-HFP/$NaPF_6$), The equivalent circuit for fitting is inserted in (a); (c) Arrhenius plots of SCE membrane (10 wt% NSSE/PVDF-HFP/$NaPF_6$) and polymer electrolyte (PVDF-HFP/$NaPF_6$); (d) Critical current density (CCD) test results of NSSE-SCE and PVDF-HFP/$NaPF_6$. (The CCD values for NSSE-SCE and polymer electrolyte are 1.1 mA cm^{-2} and 0.1 mA cm^{-2}, respectively.)

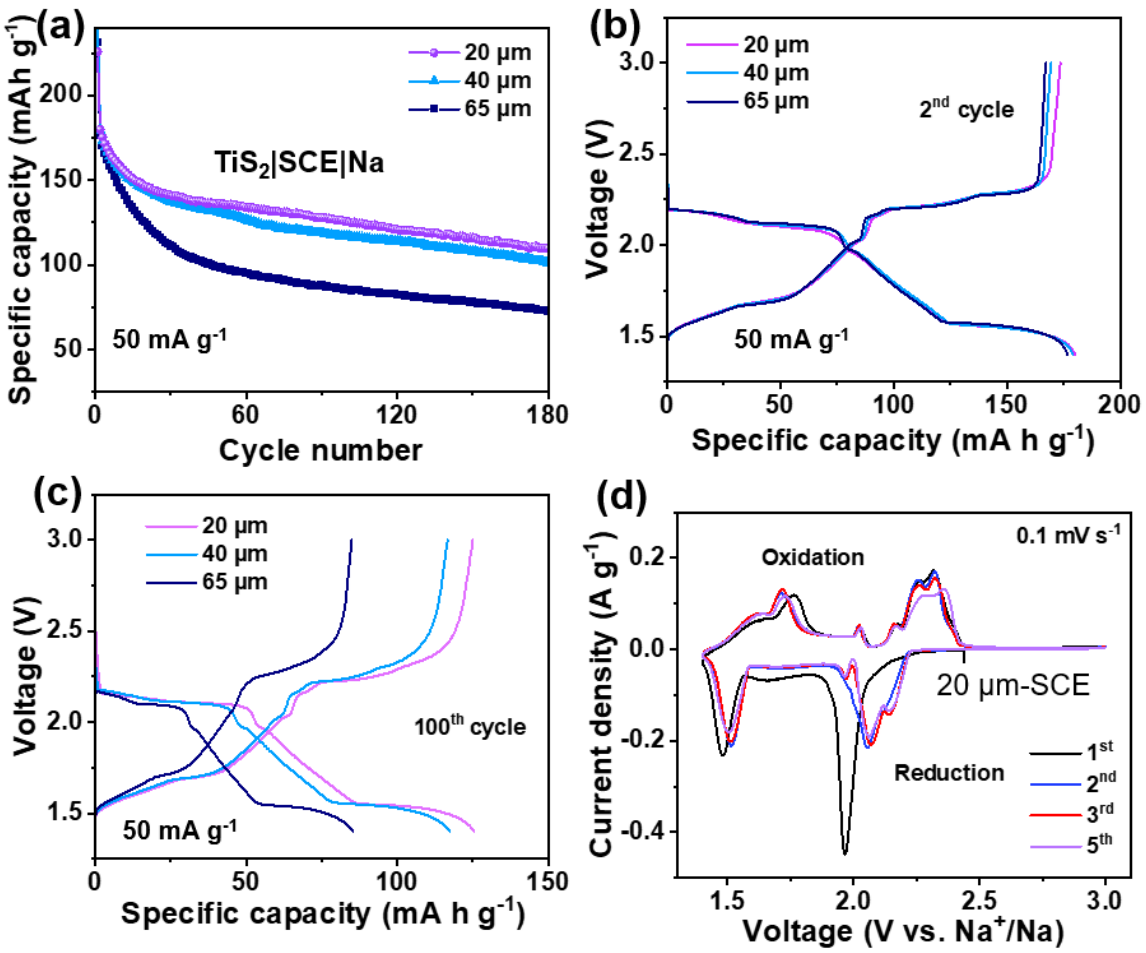

Figure 4. (a) Cycling performance of TiS_2||Na batteries using SCEs with different thickness (20 μm, 40 μm, and 65 μm); (b) and (c) Charge/discharge profiles of TiS_2|SCE|Na batteries at 2^{nd} cycle and 100^{th} cycle, respectively. (d) Cyclic voltammograms curves at scan rate of 0.1 mV s^{-1} for the cell with 20 μm NSSE-SCE.

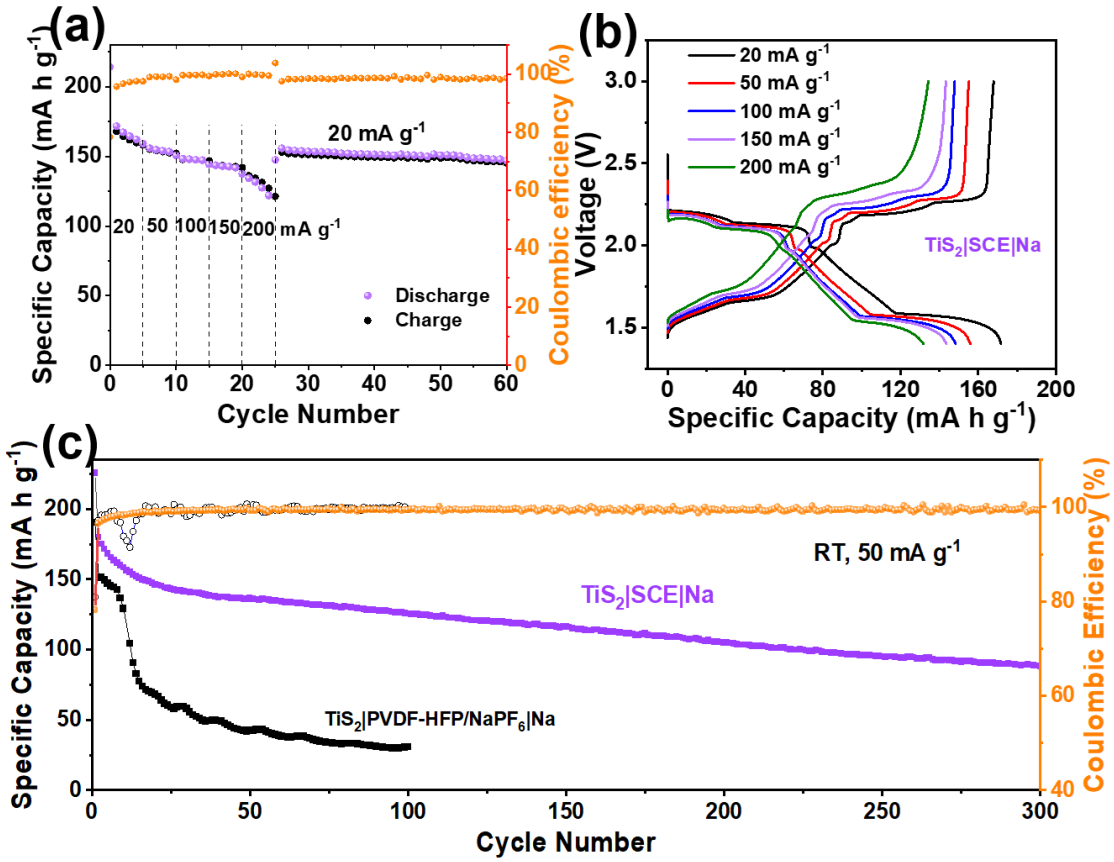

Figure 5. (a) Rate performance and (b) charge/discharge profiles of TiS_2|SCE|Na cells at the current density of 20, 50, 100, 150, 200 mA g^{-1}; (c) Long-term cycling performance of TiS_2|SCE|Na and TiS_2|PVDF-HFP/$NaPF_6$|Na. The electrochemical cycling window range is between 1.4-3.0 V (vs. Na^+/Na).

Graphical Abstract